

Performance of GO/SiO₂, GO/TiO₂, and GO/ZrO₂ Nanocomposites Coatings as a Corrosion Barrier Layer on Al-Si-Cu-Mg Alloy in 3.5 % NaCl Solution

Lamiaa Z. Mohamed^{1,*}, G. Hamdy², Ghalia A. Gaber²

¹ Mining, Petroleum and Metallurgical Engineering Department, Faculty of Engineering, Cairo University, Egypt

² Chemistry Department, Faculty of Science, Al-Azhar University (Girls), Nasr city, Cairo, Egypt

*E-mail: lamlomy@yahoo.com

Received: 18 December 2020 / Accepted: 10 February 2021 / Published: 31 March 2021

The research target aimed to design of anodic oxide film layers on Al-Si-Cu-Mg alloy by modifying phosphoric acid anodizing and reinforcement by subsequent impregnation with graphene oxide (GO) nanosheets deposition effects (SiO₂, TiO₂ and ZrO₂). The corrosion inhibition efficiency on the anticorrosion behavior of the coating layer (GO/SiO₂, GO/TiO₂, and GO/ZrO₂) nanocomposites were deposited by electro-deposition in 3.5 % NaCl solution. Complementary electrochemical measurements including estimate of weight reduction, chronoamperometric current-time and potentiodynamic polarization techniques showing the ability of the improved oxide layer with GO/ZrO₂ were more successful in preventing corrosion, which acts as a self-cleaning coating with a novelty few-layer GO nanosheets with GO/ZrO₂. The surface morphology and elemental analysis of GO/SiO₂, GO/TiO₂ and GO/ZrO₂ nanocomposites coating were evaluated by SEM, EDS and mapping of elemental distribution.

Keywords: Al-Si-Cu-Mg Alloy, Anodic oxidation, Graphene oxide, Nanocomposites, Corrosion resistance.

1. INTRODUCTION

Al-Si-Cu-Mg alloy due to their excellent strength, low cost and hardness values, is widely used in engine parts, aerospace, and construction industries, however, at some loss of ductility and resistance of corrosion [1, 2]. The alloy is very sensitive to heat treatment due to the presence of both Cu and Mg. Aluminum corrosion resistance and its alloys is derived from the durable film of oxide produced on the surface naturally. However the corrosive media surface of Al is not capable of shielding this film. The high chloride concentration of corrosive media will cause the film to break down and result in both uniform and pitting corrosion [3]. In order to enhance Al's corrosion resistance, aluminum anodization

has been extensively studied and approved as part of different techniques [1]. In several respects, anodizing Al and its alloys is used as a surface functionalization [4]. The two-layer structure of the anodizing film, a non-porous barrier oxide and a porous outer oxide [5], is generally accepted. A protective anodic aluminum oxide (AAO) film is electrochemically formed on Al substrates during the anodization process which consists of a thin compact barrier layer and a dense, porous layer. The formed oxide on the surface is used for further treatment, leading to the sealing of existing pores, for enhance the Al alloys corrosion resistance [4]. The various sealing treatments effect on the corrosion resistance of AAO film and films sealed with boiling water and potassium dichromate have been found to provide greater corrosion resistance in acid solution [6]. Also, it was investigated with hot nickel acetate that both filled the pores and deposited on the air surface were found to outperform samples sealed with other sealing methods [5]. Duplex anodic layers and silane-based sol-gel sealed them and noticed that the AA2024-T3 corrosion resistance was substantially improved. This is due to the keeping of sol-gel materials in anodized alumina phosphoric acid and the preservation of the natural hydration property of the anodized layer of sulfuric acid between the composite of sol-gel/oxide and the substratum [7]. The impregnation of the porous layer by chemical nanotechnology is an environmentally friendly choice to increase the oxide layer's corrosion resistance thus maintaining the properties of adhesion promotion.

The approach is to fill the open structural pores through a dipping process with nano-sized SiO_2 particles. The anodic layers will be strengthened if the nanoparticles fill the pores only partially, and the surface enlargement will be preserved by open porosity. However, a well-matched relationship between the particle size and the pore diameter [8] is needed for the nanoparticles incorporation. The vacuum dip-coating TiO_2 sol-gel on the anodized Al surface prepared a stable nano- TiO_2 coating and finding that this type of coating exhibited excellent corrosion resistance at room temperature in sterile seawater [9]. Graphene oxide-functional materials have recently become critical for surface defense because the electrolytes are unable to penetrate through the graphene oxide layered structure [10]. More and more focus has been drawn to graphene oxide (GO) with excellent properties [11]. A green, oil-based GO mild steel corrosion inhibitor was registered, the performance of which increased as the hydrophobicity of the coated surface improved [12]. A composite GO-polymer material that strengthened the inhibition of corrosion in mild steel was also documented, which was due to enhance hydrophobicity due to the polymer matrix [13]. In addition, in a 3.5 % NaCl solution, the acetone-derived GO was documented to act as a corrosion inhibitor for Cu. Silica nanoparticles have been used in salt environments as a corrosion barrier for the Al alloy [15]. The GO was added into the AA2024 alloy-formed sol-gel film and found that the addition of GO led to improve the sol-gel film corrosion resistance with an acceptable concentration of 0.5 mg/ml [16]. AA2024 was applied with sol-gel containing rGO@APTES nanoplates, forming defect-free, uniform, dense and adherent coatings, and clearly improved rGO@APTES nanoplates corrosion resistance with 100 ppm concentration [1, 17]. In addition, in the 3.5 % NaCl solution, many authors reported corrosion inhibition barrier layers prepared from pyridine-functionalized graphene oxides as well as GO composites with polystyrene, metronidazole, polyvinylene and lignin [18-22].

The target of the present work to evaluate the best nanoparticles and reduced graphene oxide (rGO) on SiO_2 , TiO_2 , and ZrO_2 deposited by electro-deposition which is a flexible low-cost method of fabrication. Also, to assess its corrosion inhibition activity in chloride environments in the Al-Si-Cu-Mg

alloy. It could be a promising approach to improve open porous phosphoric acid anodized layers of Al-Si-Cu-Mg alloy by adding GO nanosheets. The corrosion resistance was contrasted between AAO films after deposition of GO/SiO₂, GO/TiO₂ and GO/ZrO₂ nanocomposites and tested using different electrochemical techniques when subjected to 3.5 % NaCl solution. The surface morphology of different conditions before and after corrosion were investigated by using SEM micrographs and EDAX analysis and elemental distribution by mapping.

2. EXPERIMENTAL WORK

2.1. Materials

The investigated Al-Si-Cu-Mg alloy has the chemical composition in weight percentage of 12.76% Si, 0.14% Fe, 2.71% Cu, 0.56% Mg, 0.19% Zn, 0.03% Ti and the rest is Al. The alloy coupon was ethanol degreased, then etched in NaOH (0.5 g l⁻¹) aqueous solution for 5 min at 40 °C and eventually neutralized for 2 min at room temperature in HNO₃ (25 vol.%) [23]. The porosity of the anodic films must have a pore diameter greater than the nanoparticles one (approximately 20 nm) to allow the penetration of particles inside pores. Due to the need for large pores, Al-Si-Cu-Mg alloy was galvanostatically anodized (1.5 Adm⁻²) for 20 min in a phosphoric acid temperature-controlled bath (0.5 mol l⁻¹) where Pt sheet was used as a cathode [4]. For later usage after anodization, the samples were rinsed entirely in distilled water. GO/SiO₂, GO/TiO₂ and GO/ZrO₂ nanocomposites were deposited using the electrophoretic deposition (EPD) technique. A graphite counter electrode was used as the anode [5], in which anodized samples were set as the cathode. Particles deposition bath media were ready to be 2wt. % by diluting graphene oxide SiO₂, TiO₂ and ZrO₂ nanoparticles with ultra-pure water. The pH-value was adjusted to pH=10. The alloy was dried at the ambient temperature for subsequent use.

2.1.1. Preparation of GO/SiO₂ nanocomposite

GO/SiO₂ nanocomposite were fabricated by the hydrolysis of tetraethyl orthosilicate TEOS (Sigma Aldrich) [24]. The GO (0.3 g) was normally ultrasonically dispersed into an ethanol (ADWIC, 82 ml) and water (3.4 ml) alcohol-water mixed solution for 30 min. Then the ammonia solution (25 %, Merck, 5.6 ml) was applied and vigorously stirred as a catalyst to form stable and homogeneous suspensions. The required quantity of tetraethyl orthosilicate TEOS was subsequently rapidly added and allowed to react for 15 h at room temperature. Then the mixture was centrifuged and washed with deionized water and absolute ethanol at least 5 times each. Finally, before further use the commodity was dried under vacuum condition at 60 °C for 5 h.

2.1.2. Preparation of GO/TiO₂ nanocomposite

A round bottom flask containing 80 ml of DI water and 120 ml of isopropyl alcohol (IPA, Sigma-Aldrich) was added with GO/TiO₂ nanocomposite from GO nanosheets and titanium isopropoxide

(TTIP, 97 %, Merck) through in situ sol-gel reaction at pH = 2, 400 mg of GO nanosheets. To obtain an appropriate suspension of GO, the resulting mixture was put in a bath sonicator (40 kHz) for 1 h along with the round bottom flask. Then, 0.16 ml of titanium isopropoxide TTIP (40 wt. % of GO's total weight) in 20 ml isopropyl alcohol IPA was applied dropwise at room temperature to the suspension under stirring condition. Using 4 M HCl (Sigma-Aldrich), the pH of the resulting suspension was changed to 2 and the reaction mixture solution was continuously stirred at 60 °C overnight. A light grey gel was produced, which was dried in a vacuum oven at 60 °C for 12 h and subsequently ground using a pestle and mortar to obtain a fine GO/TiO₂ powder.

2.1.3. Preparation of GO/ZrO₂ nanocomposites

The 0.333 g of GO, prepared as indicated in the literature by the modified Hummer method [25], was dispersed in 200 ml of de-ionized water and subjected to sonication (Amp = %, Power = 840 Watt) for the first solution for 30 min. In the meantime, ZrO₂ [26] as prepared was dissolved into the solvent to generate the second solution with vigorous stirring; and then the two solutions were mixed together. After that to alter the optimum pH, 31.5 ml of 1 M NaOH solution, NaOH, Sigma Aldrich, was added dropwise into the sonicated precursor solution. The resulting mixture was stirred under 100 °C for 1 h until the color of the mixture changed into a coffee color, and this adjustment suggested the effective combination of GO with ZrO₂, separated by centrifugation. The desired product was finally positioned for 1 h in an electric furnace at 300 °C.

2.2. Corrosion of Al-Si-Cu-Mg alloy

Electrochemical tests have been made to calculate and analyze corrosion using Voltalab 40 Potentiostat PGZ301 (Germany) and Volta Master 4 software. The investigated samples, anodized aluminum oxide (AAO), anodized aluminum oxide after GO nanosheets deposition GO/ZrO₂, GO/SiO₂ and GO/TiO₂ and served as the working electrodes. A 3.5 % NaCl (Sigma Aldrich) solution was used for chemical and electrochemical testing. The all investigated samples weight-loss results of Al-Si-Cu-Mg alloy after anodizing and GO nanoparticles deposition was evaluated in 3.5 % NaCl solution for 120 h duration. The corrosion rate (CR), of Al-Si-Cu-Mg alloy after anodizing and GO nanoparticles deposition in 3.5 % NaCl solution obtained by weight-loss method at 20°C was calculated using the following Eq. 1 [27]:

$$\text{C.R. (mm/y)} = \frac{\Delta W \times K}{A \times T \times D} \quad (1)$$

Where: K = a constant (8.76x10⁴), T = time of exposure in hours, A = area in cm², ΔW = mass loss in grams, and D = density in g/cm³. The degree of surface coverage (θ) was estimated using Eq. 2:

$$\theta = \frac{W_0 - W_i}{W_0} \quad (2)$$

Where *W_i* and *W₀* are the values of weight losses of Al-Si-Cu-Mg alloy after anodizing and GO nanoparticles deposition and anodizing AAO, respectively. The inhibition efficiency *IE*% was calculated according to Eq. 3:

$$IE\% = \theta \times 100 \quad (3)$$

Then to assess the corrosion potential and corrosion current density, potentiodynamic polarization curves were performed. The working electrode was swept from 0.8 to +0.8 V at a scanning rate of 0.2 mVs⁻¹. The corrosion rate, CR, can be computed using Faraday's Law as follows Eq. 4 [28]:

$$CR (\mu\text{m}/\text{year}) = 3.3I_{corr}M/zd \quad (4)$$

Where, z = ionic charge, M = atomic weight of metal, d = density g/cm³, and I_{corr} = corrosion current density, $\mu\text{A}/\text{cm}^2$. Degrees of surface coverage (θ) in potentiodynamic measurements were calculated using Eq. 5.

$$\theta = 1 - I_{corr}/I_{corr}^{\circ} \quad (5)$$

where I_{corr}° and I_{corr} are the corrosion current densities of Al-Si-Cu-Mg alloy after anodizing AAO and anodizing GO nanoparticles deposition, respectively. The inhibitive efficiency (IE %) was calculated employing Eq. 3.

Finally, chronoamperometric Current-Time (CT) was measured. This approach applies the metal solution interface to a constant potential and calculates its electrochemical behavior as a function of time [29]. Both electrochemical measurements and immersion tests of the specimens were carried out at room temperature and open to air, in this investigation.

2.3 Morphology of Corroded alloy

The surface morphology of the corroded Al-Si-Cu-Mg alloy before and after anodizing were investigated. The scanning electron microscope (SEM) with FEI inspects S-Netherlands coupled with energy dispersive x-ray spectroscopy (EDS) and Bryker AXS-flash detector (Germany), and mapping of elemental distribution.

3. RESULTS AND DISCUSSIONS

The SEM images explore the morphology of as received Al-Si-Cu-Mg alloy surface formed during etching and de-smutting as shown in Fig. 1(a). During immersion in HNO₃, the smut layer formed in the NaOH solution was removed. Wherever the second stage was lost due either to dissolution or detachment, the surface displayed cavities. Fig. 1(b) describes the Al-Si-Cu-Mg alloy surface images while anodizing the AAO film. As will be shown, inside the middle of the AAO layer's hexagonal shape structures, a porous framework consisting of regularly arranged nanopores present on the surface is embedded. These pores are perpendicular and parallel to the surface of the barrier layer [4]. The pores diameter was about 100 nm. Figs. 1(c, d and e) provide the electrophoretic deposition (EPD) of GO/SiO₂, GO/TiO₂ and GO/ZrO₂ nanoparticles deposition, respectively in pores at pH 10. These figures exhibit a great cover on the top surface of the AAO film after the deposition effects of GO nanoparticles (SiO₂, TiO₂ and ZrO₂). The common particle size (about 20 nm) was sufficiently smaller than the common pore diameter (about 100 nm) to integrate particles into the structures of AAO pores.

When the GO is applied to the nanoparticles, the produced film tend to be smooth, compact, more uniform, homogeneous and adherent to the surface of the substrate. This phenomena appears as GO reacted covalently from the hydrolyzed GPTMS monomer with the silanol group, forming silane functionalized GO (silane-GO) linked by covalent C-O-Si bonds that filled defects and increased GO adhesion strength to adjacent GO and the film to the substrate [1].

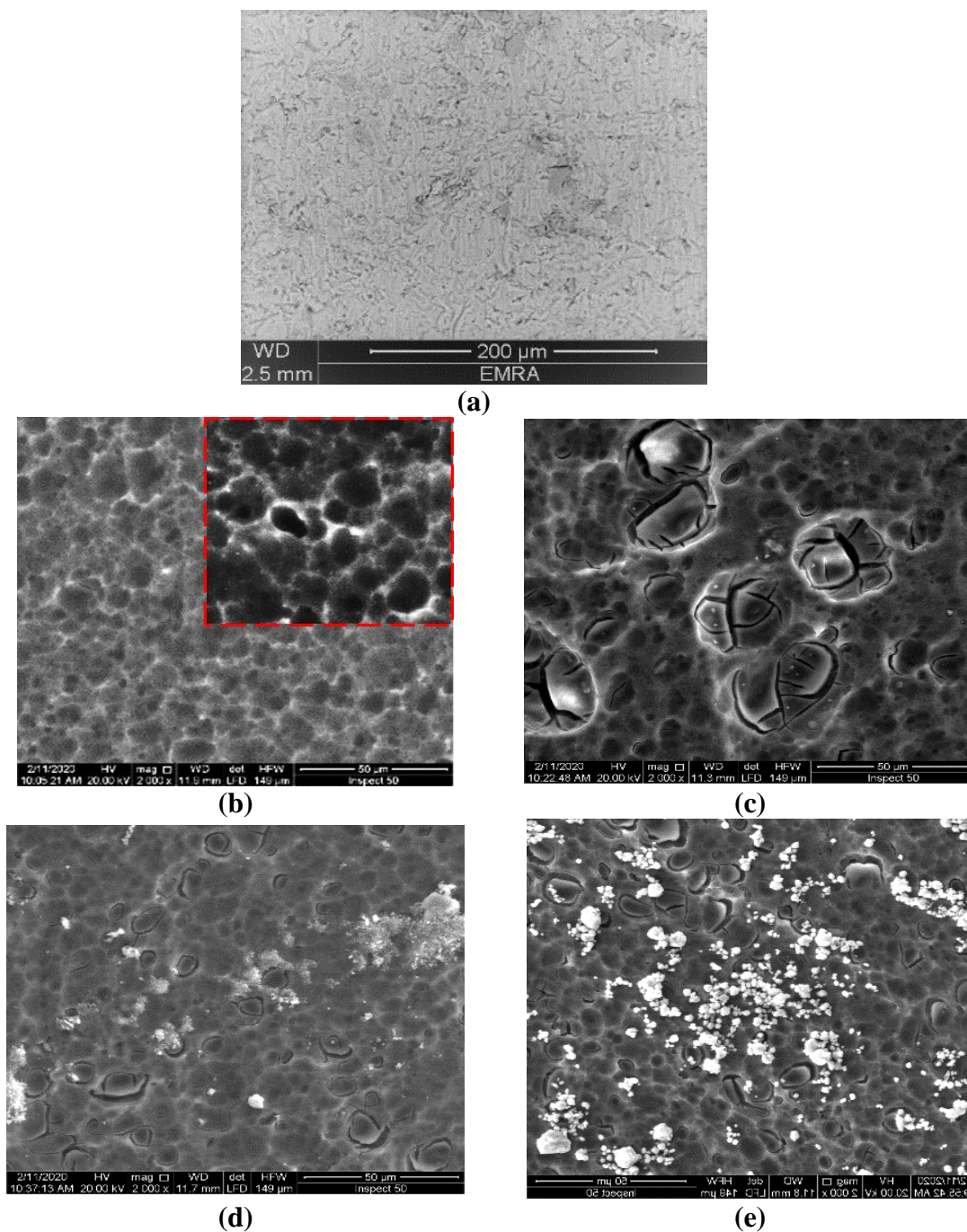


Figure 1. SEM images of Al-Si-Cu-Mg alloy surface after (a) etching, (b) anodizing AAO, (c) GO/SiO₂ deposition, (d) GO/TiO₂ deposition, and (e) GO/ZrO₂ deposition.

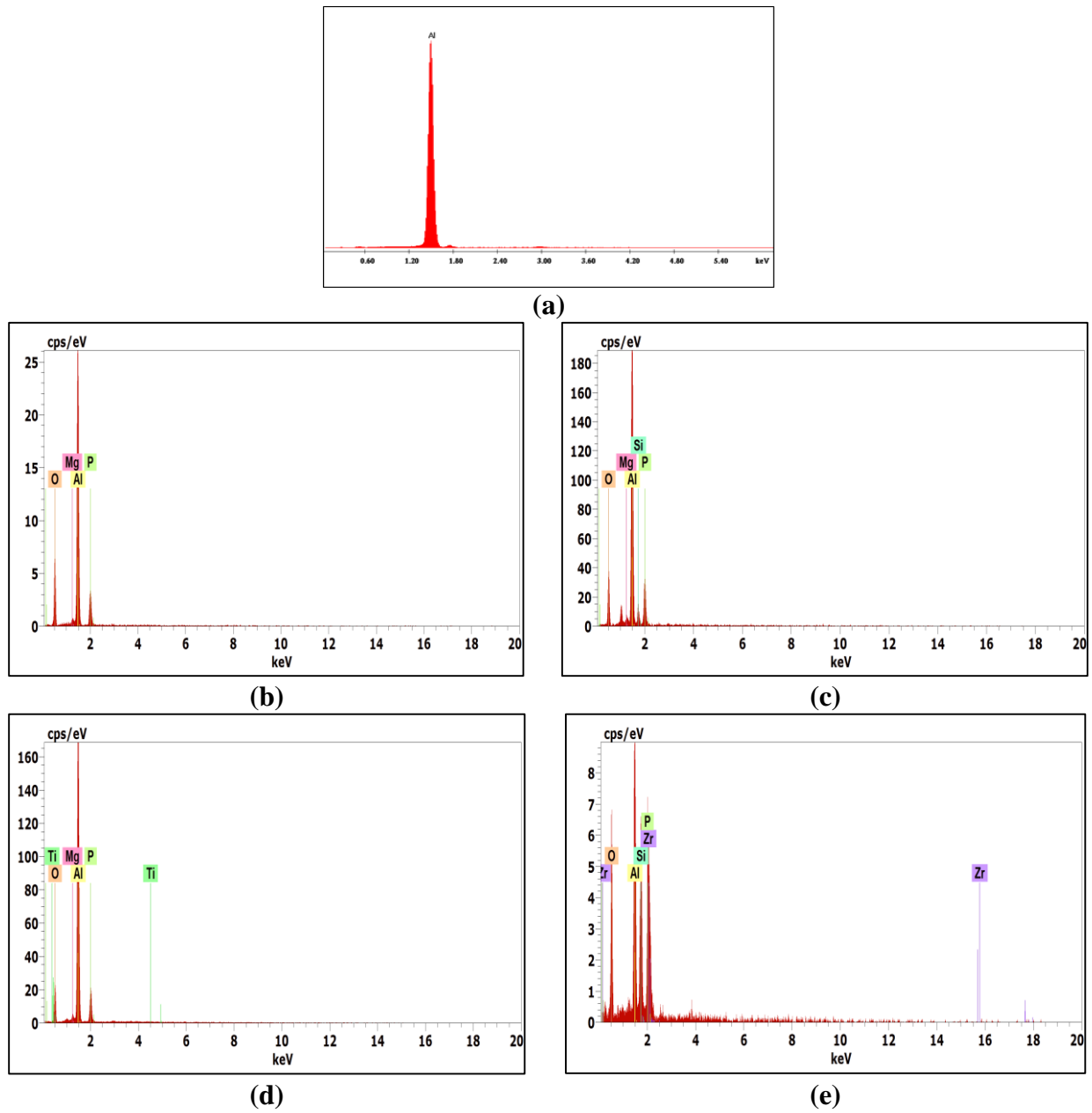


Figure 2. EDS analysis of the Al-Si-Cu-Mg alloy after (a) etching, (b) anodizing AAO, (c) GO/SiO₂, (d) GO/TiO₂, and (e) GO/ZrO₂ nanocomposites deposition.

Table 1. EDS analysis of Al-Si-Cu-Mg alloy after anodizing and GO nanosheets deposition in wt.%

Name of samples	O	P	Mg	Al	Zr	Si	Ti
AAO	41.7	11.4	0.9	46.0	--	--	--
GO/SiO ₂	36.0	11.6	1.3	47.4	--	3.7	--
GO/TiO ₂	30.2	12.2	1.1	56.4	--	--	0.1
GO/ZrO ₂	44.0	3.1	--	14.5	29.3	9.1	--

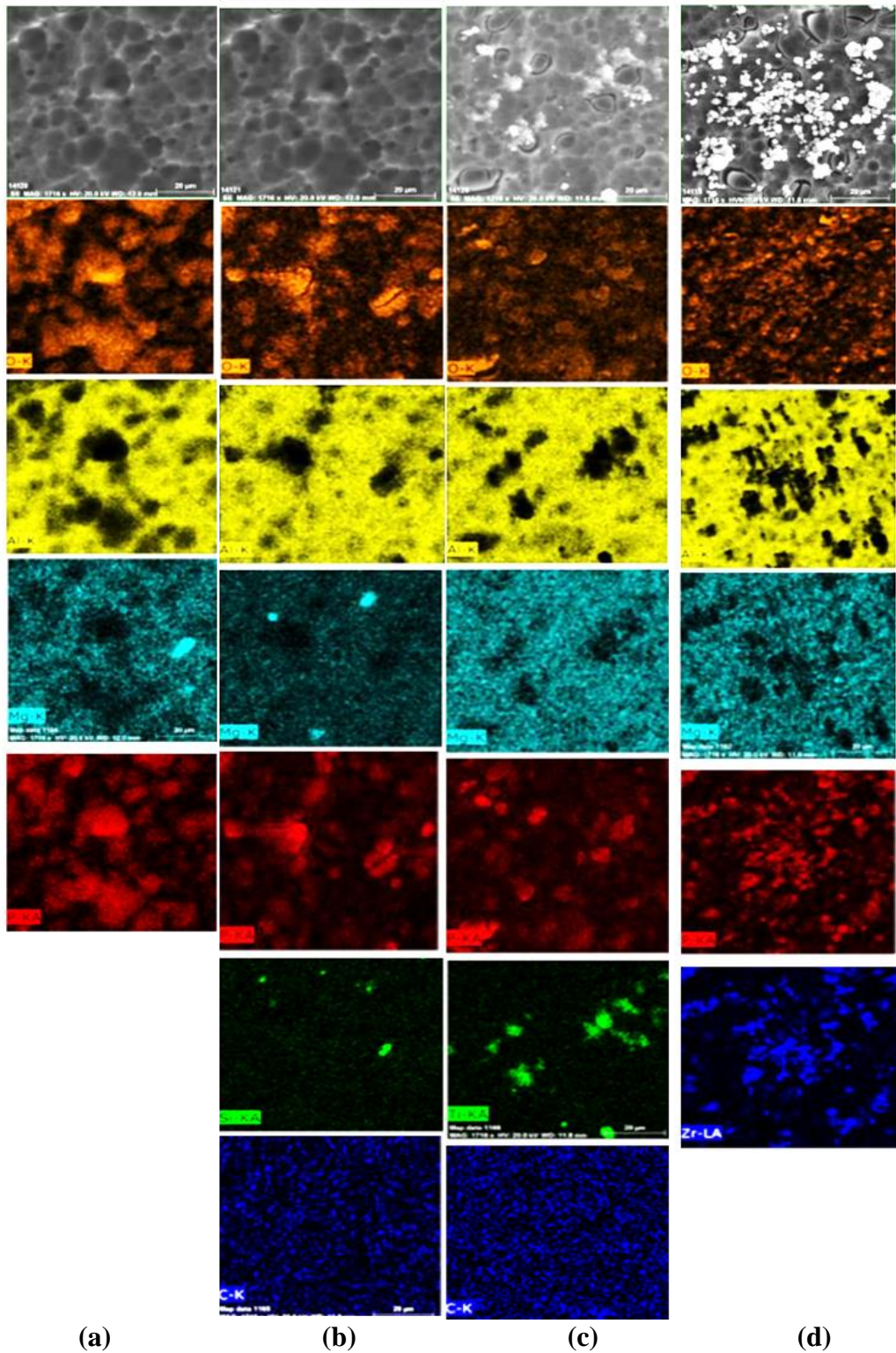


Figure 3. The mapping analysis of Al-Si-Cu-Mg alloy surface (a) after anodizing AAO, (b) GO/SiO₂, (c) GO/TiO₂, and (d) GO/ZrO₂ nanocomposites deposition.

It was formed a double-layer structure in the anodizing film, a barrier layer near the substrate is too thin (10-100 nm [13]) and a porous layer. The EDS results are conducted out the better understanding of how the GO nanoparticles covered and penetrated the porous substrate as provided in Fig. 2. The

elemental distribution by mapping for different conditions are displayed in Fig. 3. In Figs. 3(a and b) present the Al's depth profile rises from outside to inside at first and then stabilizes, but shows a sharply growing pattern close to the substrate.

While Figs. 3(c and e) give the depth profile of O decreases sharply at the interface near the substrate. The transition between the anodized film and the substrate is sharp and the composite film thickness is measured. In addition, Si and C in the EDS depth profiles are indicative of the existence of GO nanosheets. From Fig. 2(c) and Table 1 observe that Si and C atoms are confirming the deposition of uniform and thin GO/SiO₂ film on the AAO film surface. That is in strong agreement with SEM's observation in Fig. 1(c). The Si content remains relatively stable but drops significantly near the substrate, as in the anodic layer, confirming the entry of nano SiO₂ into the pores of the anodic layer. The graphene content is almost absent in the internal layer, indicating that GO does not enter the pore. It is therefore possible to treat the line between the stabilized point of Al and the sharp point of decline of graphene as the interface between the film of thin GO nanoparticles and the film of AAO [1]. The graphene content is not greater than that sealed by electrodeposition, suggesting that GO does not reach the pore [1]. The homogenous distribution of Zr than Ti and Si can be confirmed by elemental distribution by mapping in Fig. 3.

3.5. Gravimetric Measurement

The weight-loss results of the surface of Al-Si-Cu-Mg alloy after anodizing and GO nanosheets deposition immersion in 3.5 % NaCl solution for 120 h duration are demonstrated in Fig. 4. The AAO specimens experienced the highest weight losses, which the GO nanoparticles deposition specimens exhibited the lowest weight losses. However, it is also obvious that the weight-loss is generally roughly related to the chloride content in the solution. The smallest mass loss suggested that surface resistance was significantly improved by the combination of anodic oxidation and sealing. GO nanoparticles diffused into the pores during the deposition and densified the porous alumina, increasing surface resistance and reducing the mass loss of the Al alloy [36]. At the end of the immersion duration, i.e., 120h, the rate of mass loss of AAO was approximately 0.142 g cm⁻² in the 3.5 % NaCl solution, whereas it reached 0.083, 0.062 and 0.049 g cm⁻² for GO nanoparticles deposition GO/SiO₂, GO/TiO₂ and GO/ZrO₂, respectively. The weight of the AAO film was substantially greater after the same immersion time. However, depending on the result of mass loss, this film was hypothesized to be less defensive than that of the deposition of GO nanoparticles, which was possibly due to its porous structure [37]. The corresponding data inhibition efficiency, surface coverage and corrosion rate calculated from the weight-loss results for 120 h are shown in Table 2. Inspection of GO/SiO₂, GO/TiO₂ and GO/ZrO₂ nanocomposites coatings reduces the corrosion rate and showed appreciable corrosion inhibition behavior against AAO in 3.5 % NaCl solution. The GO/ZrO₂ coating onto the Al-Si-Cu-Mg alloy showed a 65.49 % increment in the corrosion inhibition activity with respect to the reference anodizing AAO, as studied.

Table 2. Corrosion rate (CR), Surface coverage (θ) and the Inhibition efficiency (IE%) of Al-Si-Cu-Mg alloy after anodizing and GO nanosheets deposition in 3.5 % NaCl solution obtained by weight-loss method at 20°C.

Samples ID	Corrosion rate (CR), (mm/y)	Surface Coverage (θ)	Inhibition Efficiency (IE %)
AAO	8.431	--	--
GO/SiO ₂	4.928	0.4155	41.55
GO/TiO ₂	3.681	0.5634	56.34
GO/ZrO ₂	2.909	0.6549	65.49

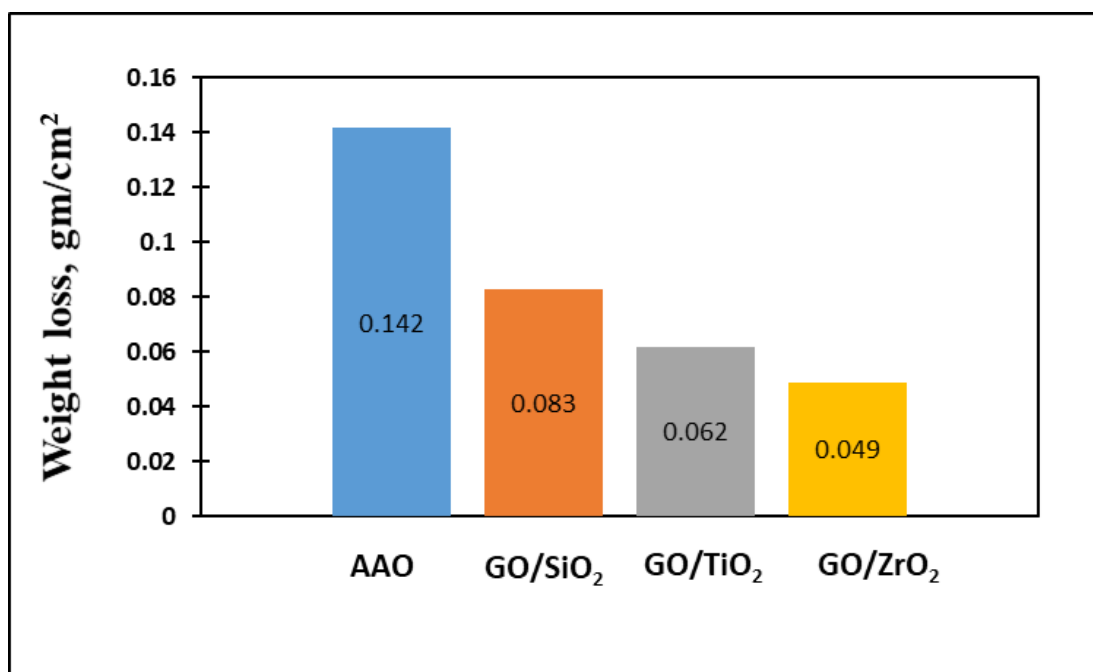


Figure 4. Weight-loss of the Al-Si-Cu-Mg alloy after anodizing and GO nanosheets deposition immersed in 3.5 % NaCl solution.

3.6. Electrochemical measurements

3.6.1. Potentiodynamic polarization measurements

The potentiodynamic polarization curves for Al-Si-Cu-Mg alloy after anodizing and GO nanoparticles deposition in 3.5 % NaCl solution are given in Fig. 5. Table 3 lists the corrosion potential (E_{corr}), corrosion current density (I_{corr}), polarization resistance (R_p), and corrosion rate (CR) values for the Al-Si-Cu-Mg alloy after anodizing and the deposition of GO nanoparticles in chloride. The polarization resistance (R_p) values were determined using Stern–Geary Eq. 6 [38]:

$$R_p = \frac{\beta_a \cdot \beta_c}{2.303 I_{corr} (\beta_a + \beta_c)} \quad (6)$$

From Table 3, the corrosion potential (E_{corr}) and polarization resistance (R_p) of GO nanoparticles deposition are greater than anodizing Al-Si-Cu-Mg alloy and corrosion current density (I_{corr}) is markedly

decreased after coating with GO/SiO₂, GO/TiO₂, and GO/ZrO₂. The calculating corrosion rate for anodizing AAO and GO nanosheets deposition GO/SiO₂, GO/TiO₂, and GO/ZrO₂ on Al-Si-Cu-Mg alloy are 0.0551, 0.0437, 0.0348, and 0.0138 mm/y, respectively. High corrosion potential, high resistance to polarization and low corrosion rate usually indicate good coating corrosion resistance [26]. Due to the porosity and weak adhesion of the anodizing AAO on the alloy surface, the corrosion potential reduced and the corrosion current are increased. Correspondingly, for the deposition of GO nanosheets (SiO₂, TiO₂ and ZrO₂), the evolution of cathodic hydrogen was regulated and the dissolution of anodic metal decreased due to the strong impermeable barrier layer on the alloy, resulting in an increase in the capacity for corrosion and a reduction in the corrosion current by one order of magnitude. For the deposition of GO/ZrO₂ nanoparticles, the corrosion inhibition performance is 74.95 % higher, revealing that it is an excellent corrosion resistant coating material for the Al-Si-Cu-Mg alloy in the chloride environment.

The corrosion potential of anodizing AAO was approximately -0.516 V and the corrosion potential of GO/SiO₂, GO/TiO₂, and GO/ZrO₂ coated samples were - 0.440 V, - 0.499 V, and - 0.493 V, respectively. On the other hand, I_{corr} is a kinetic parameter which determines the corrosion rate [39]. Fig. 5 shows the corrosion potential E_{corr} confirms the tendency. A lower cathodic current density may explain the explanation for the more negative potential of the impregnated sample, suggesting a lower reaction rate of the cathodic reaction to the impregnated sample. In addition, the corrosion potential rating must take into account the form of the graphs, which corresponds to the ideal polarizable electrode in the anodic range.

Table 3. Electrochemical parameters derived from the potentiodynamic polarization curve of Al-Si-Cu-Mg alloy after anodizing and GO nanosheets deposition in 3.5 % NaCl solution

Samples ID	E_{corr} V	I_{corr} mA/cm ²	R_p Ωcm ⁻²	CR mm/y	θ	IE %
AAO	-0.516	0.00501	24.763	0.0551	--	--
GO/SiO ₂	-0.440	0.00398	50.354	0.0437	0.2068	20.68
GO/TiO ₂	-0.499	0.00316	96.329	0.0348	0.3684	36.84
GO/ZrO ₂	-0.493	0.00126	161.085	0.0138	0.7495	74.95

The corrosion current densities measured from GO/SiO₂, GO/TiO₂, and GO/ZrO₂ nanocomposites coated on anodizing AAO was about 0.00398 mA/cm², 0.00316 mA/cm², and 0.00126 mA/cm², respectively, exhibiting a descending trend in the 3.5 % NaCl solution. Indicating that the GO nanosheets deposition diminishes appreciably the corrosion rate of anodizing Al-Si-Cu-Mg substrate. The superior stability of the deposition of GO/ZrO₂ nanoparticles [40] may be involved in the excellent corrosion resistance of the coated samples. In typical polarization curve, a lower I_{corr} and a higher E_{corr} corresponds to a lower corrosion rate and a better corrosion resistance. All investigated GO nanosheets depositions with an anodic oxide coating were polarized by better corrosion resistance parameters in comparison to AAO [23].

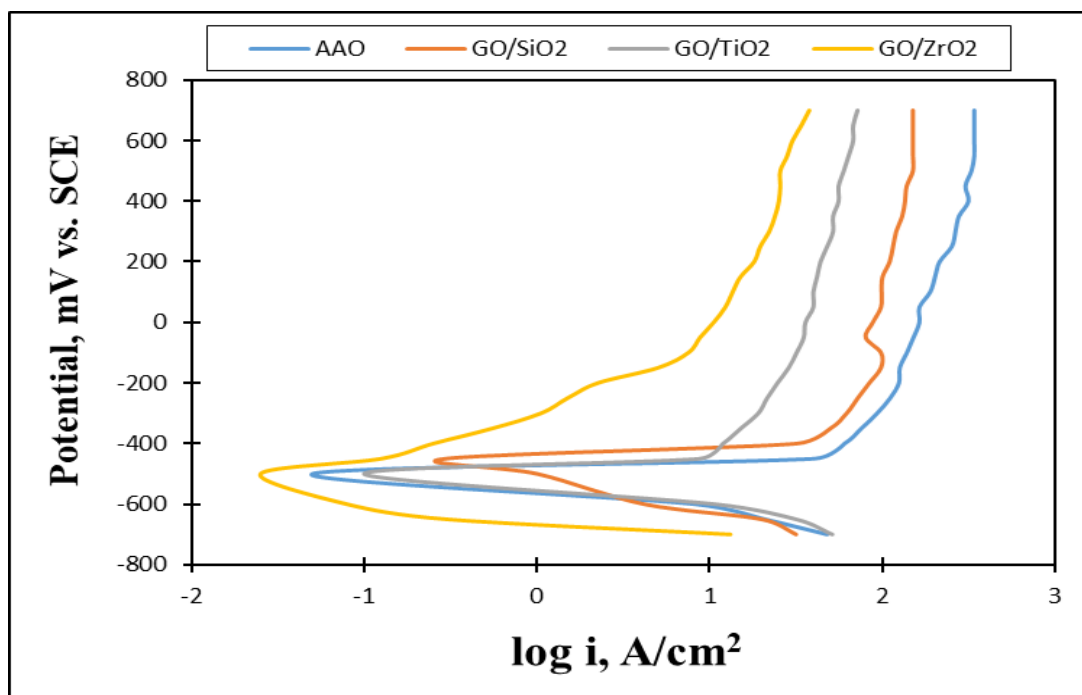
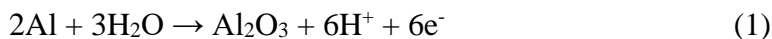


Figure 5. Potentiodynamic polarization curves for Al-Si-Cu-Mg alloy after anodizing and GO nanosheets deposition immersed in 3.5 % NaCl solution.

3.6.2. Chronoamperometric current-time (CT) measurements

Current-time (CT) experiments were also carried out to enhance the immersion time in the chloride solution by 15 min in order to shed more light on the effect of applying an active anodic potential on both uniform and pitting corrosion of SiO₂, TiO₂ and ZrO₂ deposition of AAO and GO anodizing nanosheets. Fig. 6. provides the CT curves obtained for corrosion of anodizing AAO and GO nanosheet deposition SiO₂, TiO₂ and ZrO₂ in 3.5 % NaCl solution at -0.45 V vs. Ag/AgCl. As the time of the experiment increased, the reported current for anodizing AAO showed a progressive increase in its value. On the other hand, applying this potential value, -0.45 V, to the deposition of GO nanosheets SiO₂, TiO₂ and ZrO₂ in 3.5 % NaCl solution provided low current, which decreased over time. The increase in current for the AAO sample over time reveals that Al experiences extreme pitting corrosion for 15 min at -0.45 V only after immersion in 3.5% NaCl solution. The percentage of chloride ions in the solution has been documented to actively attack the Al surface at anodic active potential, resulting in a continuous dissolution of Al through intense uniform corrosion and pitting. The formation of these Al chloride compounds accelerates the dissolution of Al itself by attacking its surface either after leaching the chloride compounds from the surface of the solution or beneath the corrosion products that lead to the formation of pits on its surface [37-41]. The AAO surface current-time CT experiments show that the Al did not experience uniform or pitting corrosion and confirm that AAO's pitting potential is more positive than -0.45 V vs. Ag/AgCl and its surface was more passivated in 3.5% NaCl solution compared to GO nanoparticles deposition SiO₂, TiO₂ and ZrO₂. This attack on the data produced by measurements of polarization, Figs. 4 and 5 confirm that extending the immersion time prior to measurement for these materials enables their surfaces to grow a top layer of oxides and/or corrosion

products that become thicker over time and thus resist the attack of chloride ions, which in turn lowers the current values obtained. During the anodic oxidation procedure, both the formation and dissolution of the oxide film occurred simultaneously on the surfaces of the Al samples [20]. Film-formation occurred in reaction (1) and film-dissolution in reaction (2). Al^{3+} escaped through the metal/oxide interface from the substrate and migrated into the oxide film, while O^{2-} was created and moved in the opposite direction of Al^{3+} at the electrolyte solution/metal interface. Once Al^{3+} met O^{2-} , the oxide film was formed.



Some Al_2O_3 of the alumina film was dissolved based on the mechanism of reaction (1) and pores were developed on the surfaces of the samples. New aluminum oxides were formed again as the electrolyte solution permeated through the pores. Films of alumina grew and then eventually spread into additional internal substrates, depending on the development and growth of the porous layer [22].

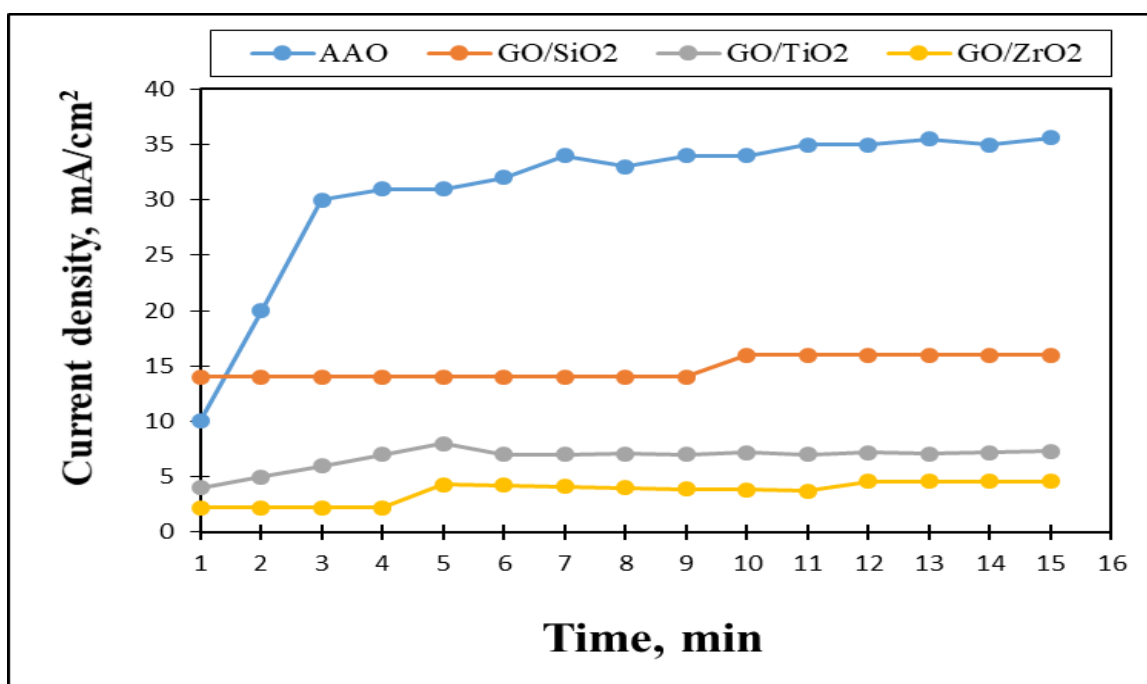


Figure 6. Chronoamperometric Current-Time (CT) curve for Al-Si-Cu-Mg alloy after anodizing and GO nanosheets deposition immersed in 3.5 % NaCl solution at -0.45 V vs. Ag/AgCl.

3.7. Surface morphology

Electrochemical experiments in the aqueous NaCl solution indicate that their passive behavior and resistance to pitting corrosion is enhanced by the impregnation of the open porous oxide layer. When the impregnation was inhomogeneous, the corrosion protection failed, or the suspension only partially penetrated into the pores due to a non-conforming dip coating process [8].

Fig. 7. displays the surface morphologies of Al-Si-Cu-Mg alloy after immersed in 3.5 % NaCl solution with anodizing AAO and deposition of GO-SiO₂, GO-TiO₂ and GO-ZrO₂. Fig. 7(a) shows the alloy surface anodizing AAO exhibits pitting and localized corrosion triggered due to barrier layer porosity and violent ion attack [18]. As represented in Figs. 7(b, c and d), the coating of GO nanoparticles have a homogeneous surface due to the corrosive ions are not allowed into the coating surface by the barrier layer [18].

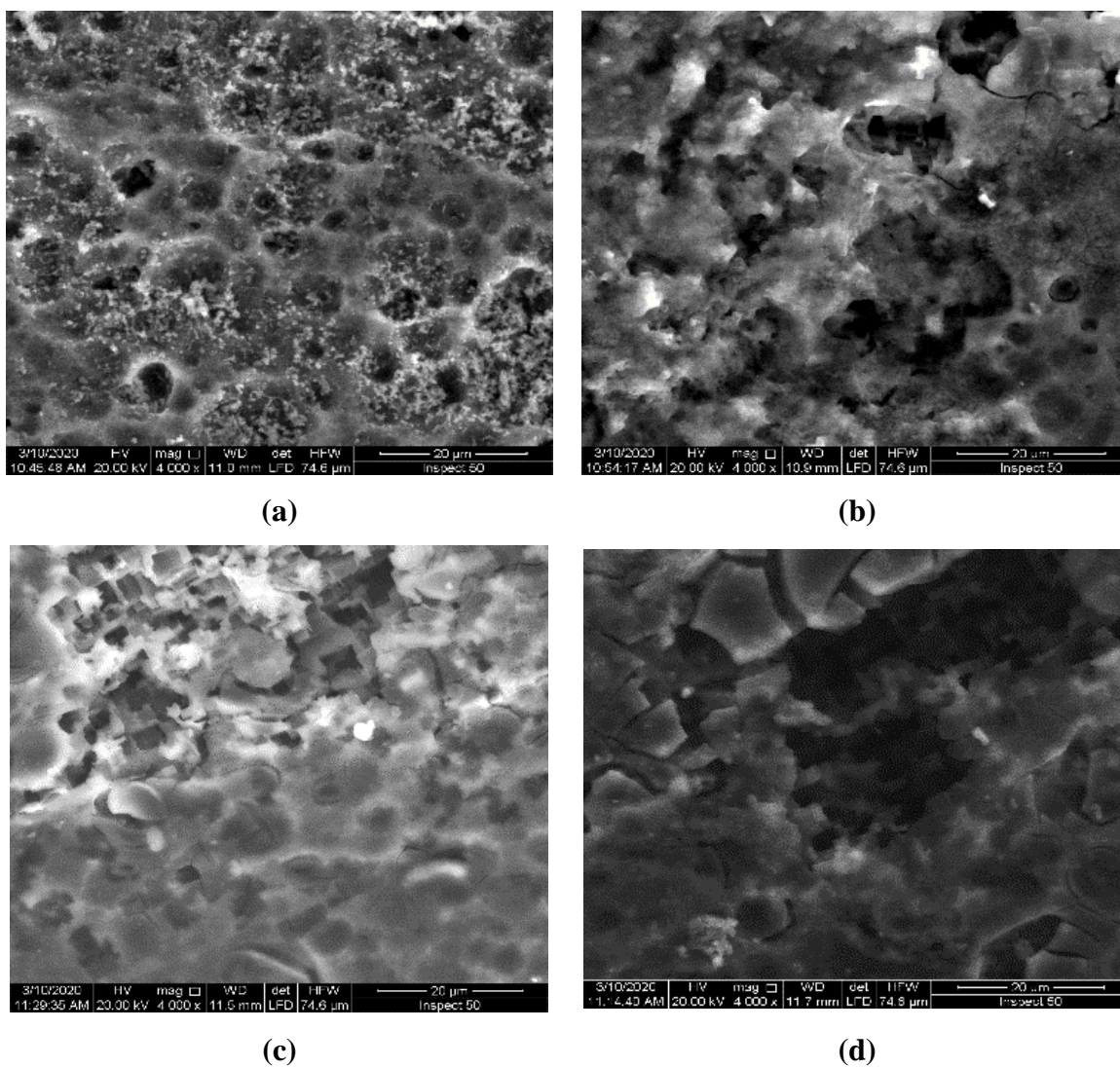


Figure 7. SEM images of Al-Si-Cu-Mg alloy surface after immersed in 3.5 % NaCl solution (a) anodizing AAO, (b) GO/SiO₂, (c) GO/TiO₂, and (d) GO/ZrO₂ nanocomposites deposition.

Thus, the heavy physisorption of the GO nanoparticles coating on the alloy surface prevent the corrosive ions to penetrate the coating surface. As indicated in the electrochemical characterization, the alloy dissolution was regulated by the impermeable GO nanoparticles on the alloy surface. Fig. 8 illustrates the morphology of the area selected and the spectrum of the EDS where elemental Si, Ti, and Zr was observed, suggesting the elementary contact with the GO. The mapping of anodizing AAO and

graphene nanoparticle deposition indicates that nanoparticle is uniformly distributed on the GO as presented in Fig. 9. The EDS results of Al-Si-Cu-Mg alloy after anodizing and GO nanoparticles deposition immersed in 3.5 % NaCl solution are shown in Table 4.

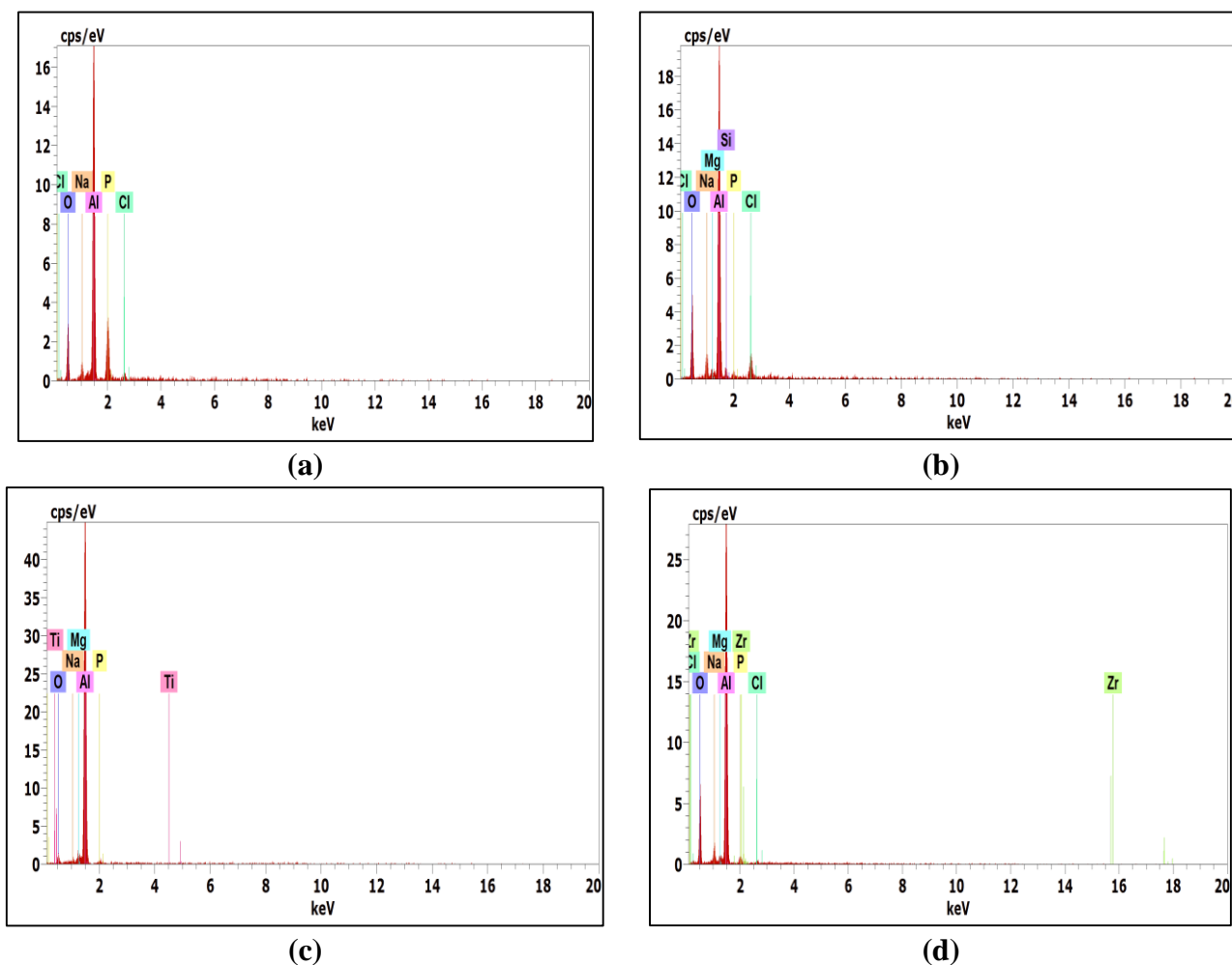


Figure 8. EDS analysis of Al-Si-Cu-Mg alloy after immersed in 3.5 % NaCl solution (a) anodizing AAO, (b) GO/SiO₂, (c) GO/TiO₂, and (d) GO/ZrO₂ nanocomposites deposition.

Table 4. The EDS analysis of Al-Si-Cu-Mg alloy after anodizing and GO nanosheets deposition immersed in 3.5 % NaCl solution in wt.%.

Samples ID	Na	Cl	O	P	Mg	Al	Zr	Si	Ti
AAO	3.0	1.2	32.8	13.5	--	49.5	--	--	--
GO/SiO ₂	4.1	5.7	39.8	1.3	0.8	46.6	--	1.8	--
GO/TiO ₂	0.4	--	12.4	0.8	1.7	84.6	--	--	0.2
GO/ZrO ₂	2.7	0.9	38.6	2.1	0.8	53.9	1.0	--	--

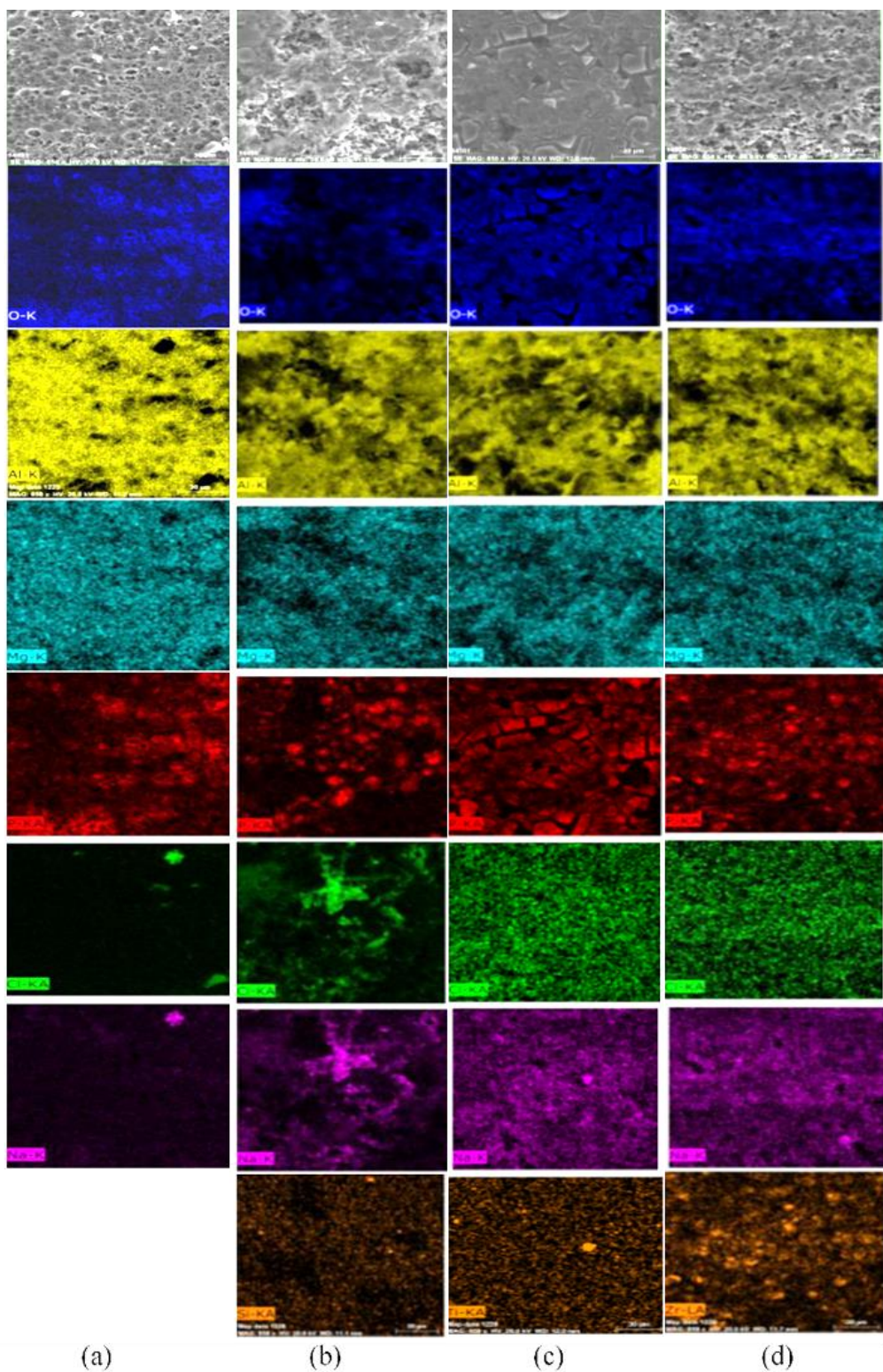


Figure 9. Mapping of Al-Si-Cu-Mg alloy after immersed in 3.5 % NaCl solution (a) anodizing AAO, (b) GO/SiO₂, (c) GO/TiO₂, and (d) GO/ ZrO₂ nanocomposites deposition.

The nanocomposites had a uniform distribution of the GO-ZrO₂ nanoparticle within the Al matrix. For alloy in Al matrix that needs to be interfaced with some note of reaction, the nano ZrO₂ particles are homogeneous distribution. As a result, as the ZrO₂ content is raised, the grain size decreases.

The precipitation that appeared was rich in Al, Zr and O. The diffusion of ZrO₂ into the Al matrix was related to the non-reaction between Al and Zr, which implies that Zr and O were partially dissolved in the diffusing alloy. In terms of molecular ZrO₂, the EDS reveals that Zr disperses in the green alloy body and that there is no ZrO₂ and Al reaction [41]. The GO/ZrO₂ particle modified coating illustrated the best corrosion protection performance, as evidenced by visual assessments through SEM and elemental mapping observations were in line with the electrochemical results.

4. CONCLUSIONS

The corrosion behavior demonstrated that the aluminum sealed by GO nanosheets had higher corrosion resistance compared to AAO, impeding the penetration into the barrier layer of corrosive environment. SEM/EDS can confirm these results because after 120 h of immersion, the samples sealed by coated GO nanoparticles had the least pitting sites. As studied by potentiodynamics, the GO/ZrO₂ coating on the Al-Si-Cu-Mg alloy showed a 74.95 % increase in corrosion inhibition activity with respect to the reference anodizing AAO. The corresponding morphology analysis revealed that the formation of pits on the alloy exhibited a porous structure with the anodizing AAO, while the surface coated with GO nanoparticles was not affected by the aggressive ions, presenting a uniform surface. Finally, it is confirmed that GO/ZrO₂ is an excellent barrier layer on Al-Si-Cu-Mg alloy in the chloride media. The Al matrix, the ZrO₂ reinforcement particles were distributed homogeneously as confirmed from visual assessments through SEM and elemental mapping observations were in line with the electrochemical results.

ACKNOWLEDGEMENT

The authors acknowledge Associate Prof. Yassar Reda (Higher Institute of Engineering and Technology Tanta) for English revision.

References

1. Y. Mei, D. Huan, S. Haobo, X. Liangliang, H. Chong, L. Jianhua, and L. Songmei, *Appl. Surf. Sci.*, 479(1) (2019) 105–113.
2. M.H. Abdelaziz, H.W. Doty, S. Valtierra, and F.H. Samuel, *Adv. Mater. Sci. Eng.*, (2018) 12–16.
3. E. S. M. Sherif, *J. Ind. Eng. Chem.*, 19(6) (2013) 1884–1889.
4. Gh.A. Gaber, W.A. Hussein, and W.A. Ghanem, *Mater. Res. Express*, 7(1) (2020) 7–13.
5. N. Hu, X. Dong, X. He, J. F. Browning, and D. W. Schaefer, *Corros. Sci.*, 97(4) (2015) 17–24.
6. Y. Zuo, P.H. Zhao, and J.M. Mao, *Surf. Coatings Technol.*, 166(2–3) (2003) 237–242.
7. M. Whelan, E. Tobin, J. Cassidy, and B. Duffy, *J. Electrochim. Soc.* 163 (5) (2016) C205–C212.
8. M. Schneider, K. Kremmer, S. K. Weidmann, and W. Fürbeth, *Mater. Corros.*, 68(10) (2017) 1090–1098.
9. T. Liu, F. Zhang, C. Xue, L. Li, and Y. Yin, *Surf. Coat. Technol.* 205 (7) (2010) 2335–2339.
10. M. Breedon, M. C. Per, I. S. Cole and A. S. Barnard, *J. Mater. Chem. A*, 2, (2014) 16660–16668.
11. D. Kang, J.Y. Kwon, H. Cho, J.H. Sim, H.S. Hwang, C.S. Kim, Y.J. Kim, R.S. Ruoff, and H.S. Shin, *ACS Nano* 6 (9) (2012) 7763–7769.
12. Y. N. Singhababu, B. Sivakumar, J. K. Singh, H. Bapari, A. K. Pramanick, and R. K. Sahu, *Nanoscale*, 7 (2015) 8035– 8047.

13. D. Dutta, A. N. F. Ganda, J. K. Chih, C. C. Huang, C. J. Tsenga, and C. Y. Su, *Nanoscale*, 10 (2018) 12612–12624.
14. J.H. Huh, S.H. Kim, J.H. Chu, S.Y. Kim, J. H. Kim, and S. Y. Kwon, *Nanoscale*, 6 (2014) 4379–4386.
15. F. Maia, J. Tedim, A. D. Lisenkov, A. N. Salak, M. L. Zheludkevich, and M. G. S. Ferreira, *Nanoscale*, 4 (2012) 1287–1298.
16. B. Xue, M. Yu, J. Liu, J. Liu, S. Li, and L. Xiong, *J. Alloys Compd.* 725 (2017) 84–95.
17. S. Nezamdoust, and D. Seifzadeh, *Prog. Org. Coat.* 109 (2017) 97–109.
18. N. Palaniappan, I. S. Cole, F. Caballero-Briones, S. Manickam, C. Lal, and J. Sathiskumar, *RSC Adv.*, 9(15) (2019) 8537–8545.
19. R. K. Gupta, M. Malviya, C. Verma, N. K. Gupta, and M. A. Quraishi, *RSC Adv.*, 7 (2017) 39063–39074.
20. Y. K. Xiao, W. F. Ji, K. S. Chang, K. T. Hsu, J. M. Yeh, and W. R. Liu, *RSC Adv.*, 7 (2017) 33829–33836.
21. Y. Deng, W. Bai, J. Chen, X. Zhang, S. Wang, J. Lin, and Y. Xu, *RSC Adv.*, 7 (2017) 45034–45044.
22. J. Di, S. Guo, L. Chen, P. Yi, G. Ding, K. Chen, M. Li, D. Lee, and A. Yan, *J. Rare Earths*, 36 (2018) 826–831.
23. A. Kozik, M. Nowak, K. Gedlek, D. Lesniak, J. Zasadzinski, and H. Jurczak, *Arch. Metall. Mater.*, 64(4) (2019) 1335–1342.
24. J. Zhu, M. Chen, H. Qu, Z. Luo, S. Wu, H.A. Colorado, S. Wei and Z. Guo, *Energy Environ. Sci.*, 6 (2013) 194–205.
25. M. Fathy, A. Gomaa, F. A. Taher, M. M. El-Fass, and A. E. H. B. Kashyout, *J. Mater. Sci.*, (2016).
26. X. Rui , C. Jiansong , Z. Shijiao , H. Shaochang , Z. Xingyu , L. Jianjun , D. Changsheng, and M. Jingtao, *Ceram. Int.*, 45(2019) 19627–19634.
27. R. Khandelwal, SK. Arora, and SP. Mathur, *E-J Chem*, 3 (2011) 1200–1205.
28. W. A. Ghanem, I. M. Ghayad, and Gh. A. Gaber, *Int. J. Metall. Mater. Sci. Eng.*, 3(5) (2013) 1–8.
29. W. Hu, J. Xu, X. Lu, D. Hu, H. Tao, P. Munroe, and Z. Xie, *Appl. Surf. Sci.*, 368 (2016) 177–190.
30. Y. S. Hu, R. Demir-Cakan, M. M. Titirici, J. O. Muller, R. Schlogl, and M. Antonietti, *J. Maier, Angew. Chem., Int. Ed.*, 47 (2008) 1645.
31. D.C. Marcano, D.V. Kosynkin, J.M. Berlin, A. Sinitskii, Z. Sun, A. Slesarev, L.B. Alemany, W. Lu, and J.M. Tour, *ACS Nano* 4(8) (2010) 4806–4814.
32. Q. Zhang, Y. Zhang, H. Li, C. Gao, and Y. Zhao, *Appl. Catal. A*, 466 (2013) 233–239.
33. F. Heshmatpour, and R.B. Aghakhanpour, *Adv. Powder. Technol.*, 23(1) (2012) 80–87.
34. S. Shukla, S. Seal, R. Vij, S. Bandyopadhyay, and Z. Rahman, *Nano. Lett.*, 2(9) (2002) 989–993.
35. R. Pawar, V. Khare, CS. Lee, *Dalton Trans.*, 43(33) (2014) 12514–12527.
36. Y. Wan, H. Wang, Y. Zhang, X. Wang, and Y. Li, *Int. J. Electrochem. Sci.*, 13(2) (2018) 2175–2185.
37. Q. N. Song, N. Xu, Y.F. Bao, Y.F. Jiang, W Gu, Z. Yang, Y.G. Zheng, and Y.X. Qiao, *J. Mater. Eng. Perform.*, 26(10) (2017) 4822–4830.
38. Gh. A. Gaber, H.A. Aly, and L.Z. Mohamed, *Int. J. Electrochem. Sci.*, 15 (2020) 8229 – 8240.
39. E. Kusmierik, *Electrocatalysis*, 11(5) (2021) 555–566.
40. Z. Ding, Q. He, Z. Ding, C. Liao, D. Chen, and L. Ou, *Nanomaterials*, 9(5) (2019).
41. M.S. Abd-Elwahed, A.F. Ibrahim, and M.M. Reda, *J. Mater. Res. Technol.*, 9(4) (2020) 8528–8534.